BIO Integration

Original Article

Ultrasound-Launched Targeted Nanoparticle Enhances Antibacterial Sonodynamic Therapy for Effective Eradication of *Pseudomonas aeruginosa* Biofilm

Lei Xin[1,a], Jiaxin Shen[1,a], Zixuan Huang[2], Jifan Chen[1,3], Tao Lin[1], Hongjian Chen[1,4], Liuhong Shi[1], Guowei Wang[1,3,*] and Pintong Huang[1,3,4]

Abstract

Infections caused by *Pseudomonas aeruginosa* biofilm significantly endanger human health worldwide. Biofilms are closely associated with antibiotic resistance because biofilms significantly undermine the efficacy of antibiotics. A novel ultrasound-launched targeted nanoparticle was developed to universally destroy biofilm, target bacteria, deliver antibiotics, and efficiently kill bacteria via ultrasonic cavitation and antibacterial sonodynamic therapy. The nanoparticle consisted of poly (lactic-co-glycolic acid) loading ciprofloxacin and perfluoropentane with a bacteria-targeted antibody installed on the nanoparticle for binding to specific bacteria. The nanoparticle exhibited a sensitive response to ultrasound and the rapid liquid-gas phase transition of perfluoropentane resulted in a cavitation effect that destroyed the extracellular polymeric substances of the biofilm and allowed deep penetration of the antibiotics. In addition, ciprofloxacin induced additional reactive oxygen species production under ultrasound stimulation, leading to an enhanced bactericidal effect and potent anti-infective activity *in vivo*. This study presents an effective strategy to tackle the extracellular polymeric substance barriers for overcoming antibiotic resistance and removing a biofilm.

Keywords

Antibacterial sonodynamic therapy, biofilms, extracellular polymeric substances, *Pseudomonas aeruginosa*, ultrasonic cavitation.

[1]Department of Ultrasound in Medicine, The Second Affiliated Hospital of Zhejiang University School of Medicine, Zhejiang University, Hangzhou 310009, China

[2]State Key Laboratory of Fluid Power and Mechatronic Systems, School of Mechanical Engineering, Zhejiang University, Hangzhou 310030, China

[3]Research Center of Ultrasound in Medicine and Biomedical Engineering, The Second Affiliated Hospital of Zhejiang University School of Medicine, Zhejiang University, Hangzhou 310009, China

[4]Research Center for Life Science and Human Health, Binjiang Institute of Zhejiang University, Hangzhou 310053, China

[a]These authors contributed equally to this work.
*Correspondence to:
Guowei Wang,
E-mail: wangguowei@zju.edu.cn

Received: January 1 2024
Revised: February 15 2024
Accepted: March 13 2024
Published Online: April 10 2024

Available at:
https://bio-integration.org/

Introduction

Biofilms contribute significantly to many infectious diseases [1]. Biofilms are easily formed on the surfaces of organs and implants, such as bone, teeth, urethra, catheters, indwelling stents, and contact lenses, resulting in a variety of complicated infectious diseases [2, 3]. Infections involving biofilms are conventionally treated with high concentrations of antibiotics, potentially leading to serious drug resistance. Antibiotic resistance was described as a major threat to human society by the World Health Organization [4]. Pathogens that are especially associated with antibiotic resistance have been described as "ESKAPE" organisms, with the letters of the acronym indicating the first letters of *Enterococcus faecium*, *Staphylococcus aureus*, *Klebsiella pneumoniae*, *Acinetobacter baumannii*, *Pseudomonas aeruginosa*, and *Enterobacter*, respectively [5]. Of these, *P. aeruginosa* has become a model bacterium for biofilm research [6]. Biofilms are formed from the aggregation of bacteria into dense communities as a protection against harsh environmental conditions [7]. Approximately 10%–25% of biofilm components consist of cells, while the remaining 75%–90% represent a matrix formed by extracellular polymeric substances (EPSs) [8]. This EPS matrix acts as a barrier, endowing the biofilm with mechanical strength, as well as protecting the bacteria from the immune response of the host. The biofilm barrier also impedes drug access, resulting in the development of antibiotic resistance of the bacteria and presenting a significant challenge for the elimination of the biofilm and effective treatment of the infection [9].

This finding has led to intensive research into the problems presented by biofilms, which can be essentially classified into two types. First, biofilm reduction has been investigated using surface treatments combined with various additives, including

inhibitory agents, antimicrobial factors, and nanostructures [10–13]. Unfortunately, these passive techniques are unable to destroy established biofilms. The second approach involves the active removal of biofilms on contaminated surfaces, which has shown limited efficacy. Regardless of which method is used, the active removal of a biofilm must address two key points. First, due to the barrier effect of EPSs, the permeability of the biofilm must be increased to allow sufficient penetration of the antibacterial agent to kill the bacteria within the EPS. Second, for precise treatment, the antibacterial agents should be specifically targeted and transported to the biofilm location.

Ultrasound (US) therapy is more effective than phototherapy because US penetrates to depths >5 cm beneath the skin without impedance by the skin and connective tissue [14, 15]. Due to its safety, US is also widely used in biomedical imaging applications [16, 17]. Currently, the most frequently used form of US therapy is sonodynamic therapy (SDT), in which sonosensitizers induce the generation of ROS through a cavitation effect [18, 19]. Compared to photodynamic therapy (PDT) and photothermal therapy (PTT), which are restricted to the treatment of skin infections and injuries, SDT is able to penetrate deep within tissues in a non-invasive manner and can treat deep-rooted infections with minimal systemic toxicity [20–23]. SDT uses low-frequency US for activation of the sonosensitizer, leading to ROS production and consequent bacterial destruction [24]. SDT has been shown to be effective against most bacteria. Ciprofloxacin (CIP), a fluoroquinolone antibacterial drug, has remarkable sonosensitivity [25]. It is possible to reuse older antibiotics in novel nano-based drug delivery systems [26]. Nanoparticles loaded with antibiotics can be used to target and deliver a drug to bacteria. Such systems have significant advantages over traditional usage, such as greater stability, controlled release of the drug, targeting ability, and enhanced bioavailability [27].

Furthermore, perfluoropentane (PFP) can undergo a liquid-gas phase transition under US irradiation, allowing the use of US in nano-sized materials [28]. This process involves encapsulation of the liquid perfluorocarbon within a shell because the liquid has a low boiling point and can readily undergo superheating and consequent vaporization [29]. Variations in pressure caused by US stimulation result in vaporization of the liquid and conversion of the droplets into gas bubbles [30]. The combination of ultrasonic cavitation and antibacterial sonodynamic therapy under US irradiation offers potential for biofilm treatment.

This study describes the design of biofilm-targeted phase-shift antibiotic-poly (lactic-co-glycolic acid) [PLGA] (TCPN) nanoparticles, as shown in **Scheme 1**. These PLGA nanoparticles were loaded with CIP and PFP using a single-emulsion technique coupled with a bacteria-targeting antibody through NHS/EDC cross-linking. US triggered the generation of microbubbles, resulting in acoustic cavitation and destruction of the biofilm EPS. At the same time, the TCPN nanoparticles released the sonosensitizer antibiotic

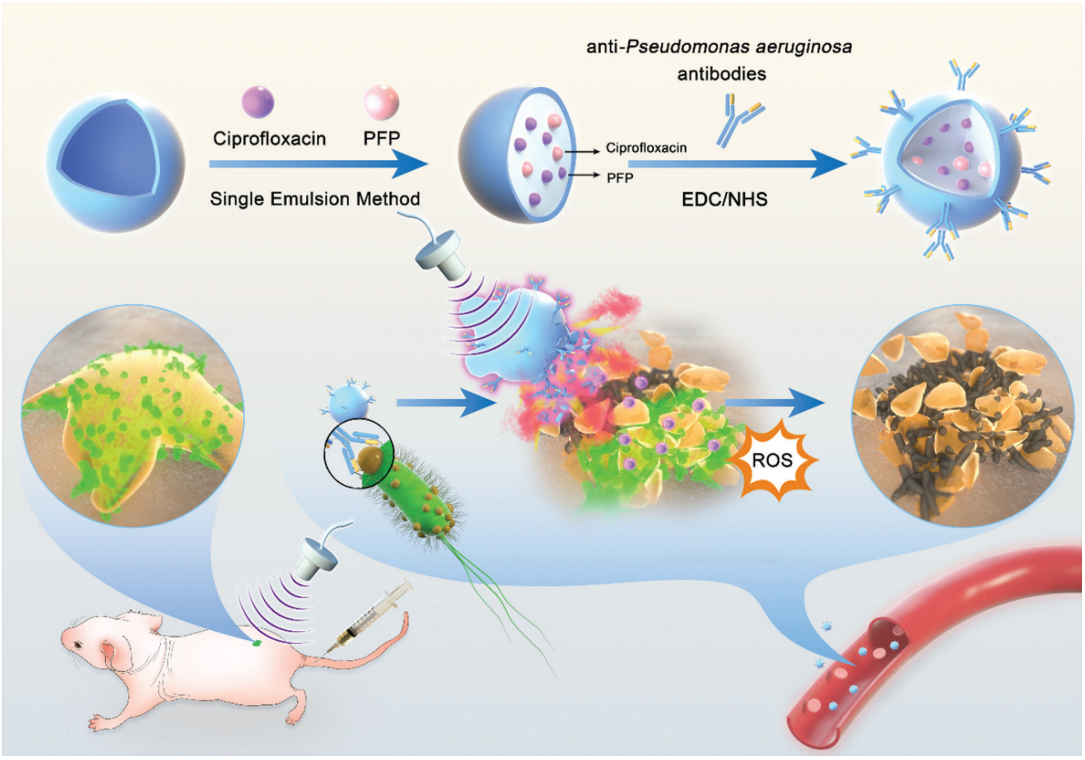

Scheme 1 Schematic diagram of the ultrasound-stimulated phase-shift nanoparticle drug delivery system for biofilm therapy. TCPN nanoparticles composed of PLGA, antibiotics (CIP), and PFP were prepared via a single-emulsion method, following conjugation with the antibodies specific for *Pseudomonas aeruginosa*. After intravenous injection, TCPN is stable in the bloodstream and can be delivered to the wound sites via the homing of anti-*P. aeruginosa* antibodies. Once triggered by US irradiation, TCPN are transformed into microbubbles via PFP phase-shift, resulting in acoustic cavitation and destruction of the EPS of biofilms. TCPN can release the sonosensitizer antibiotic, CIP, which will produce additional ROS, enhance bacterial killing, and accelerate wound healing.

(CIP), produced ROS, enhanced bacterial killing, and accelerated wound healing. This system was shown to increase the accuracy and tissue penetration of drug delivery, providing a promising method to kill *P. aeruginosa* and eliminate the biofilm.

Results and discussion

Preparation and characterization of TCPN nanoparticles

TCPN nanoparticles were prepared using a single emulsion and solvent evaporation, and were coupled with P. *aeruginosa*-specific antibody (B11) by carbodiimide conjugation. The TEM and SEM images of TCPN are shown in **Figure 1A and B**, respectively. The TCPN morphology was shown to be regular, spherical, and evenly distributed with no apparent aggregation. Under US irradiation, the TCPN underwent a liquid-gas phase transition and was transformed into microbubbles with a particle size of approximately 1198.5 ± 25.8 nm, as shown in **Figure 1C and D**. Under storage conditions at 4°C, the particle sizes and zeta potentials of the TCPN were measured several times for 21 days, as shown in **Figure 1E and F**. The results showed no significant changes in either parameter, indicating that the TCPN had good stability. The average particle sizes, PDIs, and zeta potentials of TCPN, CPN, and CN measured by DLS are shown in **Figure 1G**. The TCPN particle size was 205.9 ± 47.7 nm, with a PDI of 0.038, and a zeta potential of −27.1 ± 0.3 mV, indicating good dispersibility. The results of DLS measurements were consistent with the electron microscopy results. The average particle size of TCPN was slightly larger than the CPN nanoparticles, which indicated successful antibody coupling. The encapsulation efficiency of TCPN measured by UV spectrophotometry was 56.0% and the drug loading was 9.0%.

Conjugation of the anti-*P. aeruginosa* antibody (B11) to the CPN nanoparticles was confirmed by incubation with a FITC-labeled secondary antibody. As shown in the CLSM results in **Figure 1H**, the DiI-labeled TCPN showed red fluorescence, while binding of the FITC-labeled secondary antibody was indicated by green fluorescence. It was apparent that the red and green fluorescence fused with yellow fluorescence using the fusion channel, indicating that the secondary antibody specifically recognized the B11 antibody on the surfaces of the TCPN. This finding demonstrated the successful coupling between the CPN and the anti-*P. aeruginosa* antibodies.

The CD spectra of TCPN are shown in **Figure 1I**. CD spectroscopy is a sensitive method for the determination of protein structure. The CD spectrum showed the presence of a negative band at 200–250 nm in TCPN, which is consistent with the negative band of the anti-*P. aeruginosa* antibody (B11). FTIR spectra were acquired in the vibration frequency range of 1500–2000 cm^{-1}. Based on the FTIR spectrum (**Figure 1J**), TCPN shared the same characteristics as the anti-*P. aeruginosa* antibody (B11). The peak at 1680 cm^{-1} in TCPN represents the formation of amide bonds. Thus, both CD and FTIR spectroscopy confirmed that the anti-*P. aeruginosa* antibody (B11) was successfully coupled to TCPN.

Detection of ROS generation in TCPN nanoparticles

Bacterial biofilms are resistant to antibiotics and immune factors, making bacterial biofilms difficult to eradicate and likely leading to various chronic bacterial infections. It has been reported that PDT can eliminate bacterial biofilms associated with infected wounds and dental caries. However, because light only penetrates to relatively shallow depths, it is more challenging to eliminate biofilms in deep wounds. Acoustic dynamic therapy can be applied to various depths of biofilms.

To investigate the mechanism underlying bacterial death, changes in ROS levels within the bacteria were investigated using the cell-permeable fluorescent probe, DCFH-DA. DCF is an oxide of DCFH that emits green fluorescence, indicating ROS generation. The intensity of DCF fluorescence was used to assess the optimal US parameters for biofilm treatment, including ultrasound intensity, duty cycle, and frequency (**Figure 2A-C**). Increased ultrasound intensity leads to prolongation of the duty cycle and an increase in frequency, resulting in increased ROS generation. The optimal US parameters were shown to be an ultrasound intensity of 1.5 W cm^{-2} duty cycle of 50%, a frequency of 1 MHz, and a treatment time of 10 min. As shown in **Figure 2E**, there was almost no green fluorescence in the control, CIP, and CIP+US groups, while strong green fluorescence was noted in the TCPN+US group, indicating that the sound-sensitive agent CIP loaded in the TCPN effectively produced ROS in bacterial cells when stimulated by US. **Figure 2D** shows the semi-quantitative analysis of fluorescence. ROS can cause oxidative damage to bacterial cell membranes and disrupt various physiologic processes, leading to bacterial death. Thus, TCPN demonstrated superior acoustic dynamic effects, generating ROS and killing bacteria.

In vitro antibiofilm effect

As is well known, pathogenic bacteria are prone to infecting skin wound tissues and tend to form biofilms composed of EPSs and bacteria, thereby preventing the process of skin wound repair. Due to the barrier properties of EPSs, drugs, including conventional antibiotics, have difficulty penetrating the biofilm, thus decreasing the effective concentrations of the drugs in the wound tissues. *P. aeruginosa* is a Gram-negative bacterium that is frequently used as a model pathogen in biofilm research. Therefore, *P. aeruginosa* was selected in this study for biofilm preparation in *in vitro* experiments, and the antibacterial and anti-biofilm properties of the nanomaterials were analyzed.

The biomass of the *P. aeruginosa* biofilm was quantitatively analyzed in *in vitro* experiments by measuring the OD of the biofilm after staining with crystal violet (**Figure 3A**).

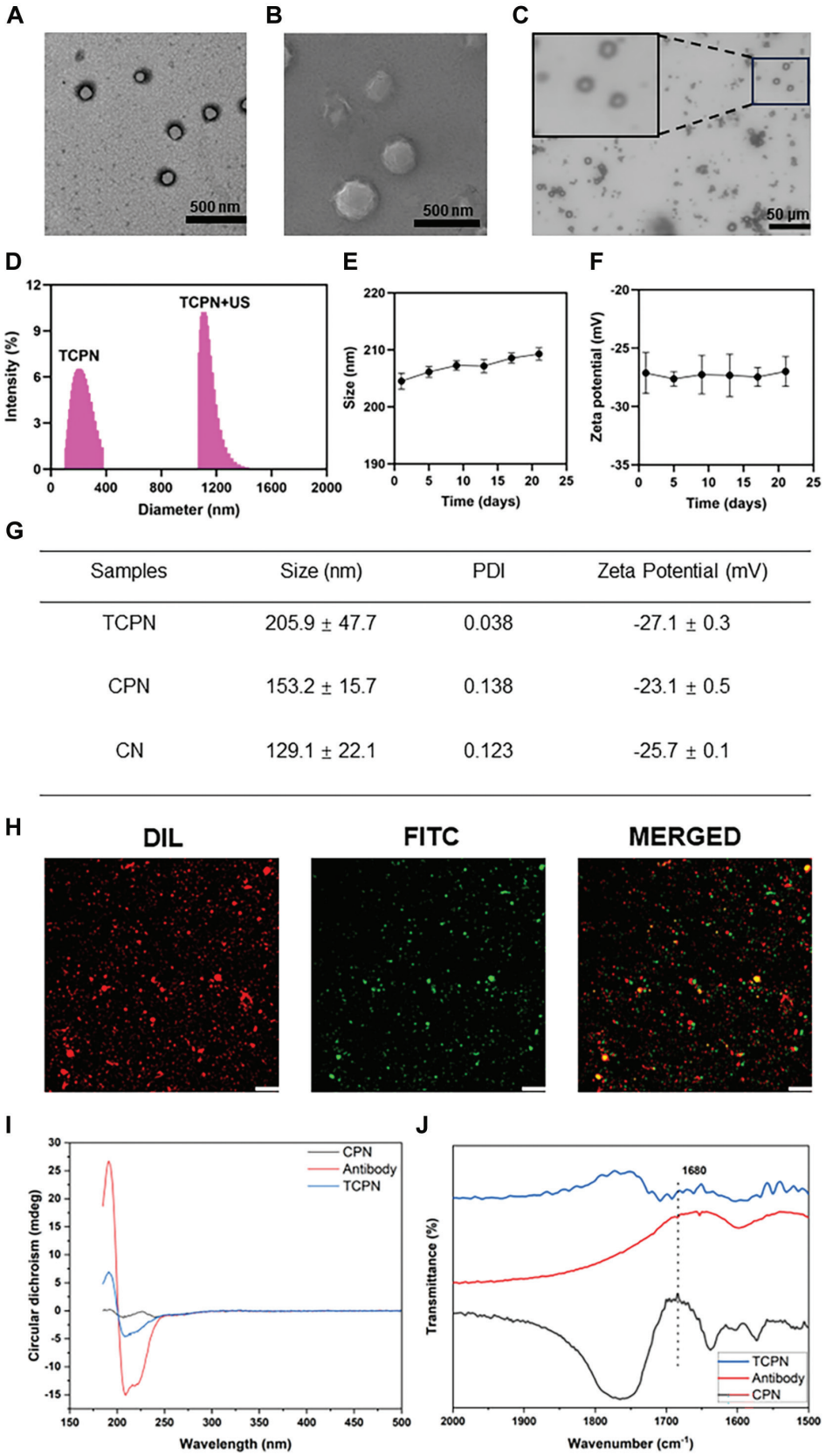

G

Samples	Size (nm)	PDI	Zeta Potential (mV)
TCPN	205.9 ± 47.7	0.038	-27.1 ± 0.3
CPN	153.2 ± 15.7	0.138	-23.1 ± 0.5
CN	129.1 ± 22.1	0.123	-25.7 ± 0.1

Figure 1 Characterization of TCPN and its antibody modification. A) TEM image of TCPN. Scale bar = 500 nm. B) SEM image of TCPN. Scale bar = 500 nm. C) Microbubbles transformed from TCPN after US irradiation. Scale bar =50 μm. D) Size distributions of TCPN and TCPN under ultrasound measured by DLS. E) Average sizes and F) zeta potentials over 21 d of TCPN. Data represent means ± SD, n = 3. G) Average sizes, PDI values, and zeta potentials of TCPN, CPN, and CN. H) Fluorescence images of DiI-labeled TCPN and FITC-labeled secondary antibody, captured by CLSM. Scale bar = 50 μm. I) CD and J) FTIR spectra of TCPN, CPN, and anti-*Pseudomonas aeruginosa* antibody.

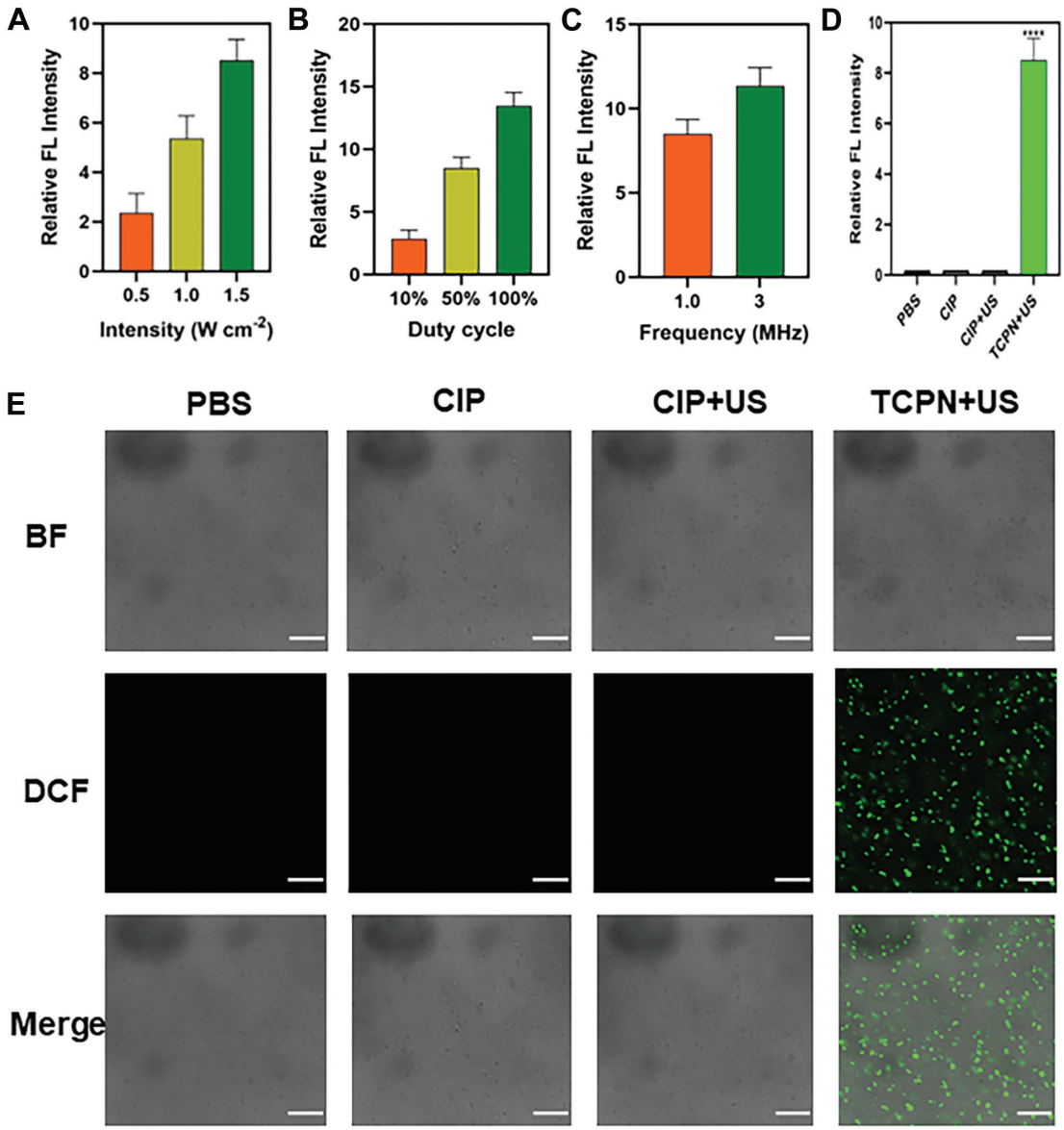

Figure 2 Semi-quantitative measurement of ROS by DCF fluorescence in the biofilm. After different treatments, levels of ROS vary with the ultrasound parameters A) intensity, B) duty cycle, and C) frequency. D) The relative level of ROS detected by DCF fluorescence in PBS, CIP, CIP+US, and TCPN+US group. E) The ROS level in biofilms shown by DCF fluorescence under different treatments. The US parameters were as follows: 1.5 W cm^{-2} intensity; 50% duty cycle; 1 MHz frequency; and 10 min duration. Images, from top-to-bottom, show the BF channel, the DCF channel, and a merge of the two channels. Scale bar = 20 μm. Data represented as the mean ± SD and analyzed by one-way ANOVA. Statistical significance: ****P<0.0001.

It was found that relative to the control group, the biomass of the biofilm in the CIP, CIP+US, and CN+US groups decreased by 15%, 16%, and 22%, respectively. However, in the CPN+US group, a decrease of 58% was measured and in the TCPN+US group a decrease of 95% occurred. This finding demonstrated that the TCPN+US group had the best scavenging effect on the biofilm.

Further *in vitro* experiments assessed the activity of biofilms by XTT metabolism (**Figure 3B**). In the CIP and CIP+US groups, the activity of the biofilms was inhibited by 8% and 12%, respectively, which may be related to the inability of drugs alone or US-treated drugs to kill bacteria tightly encapsulated in biofilms. An inhibition of 21% was observed in the CN+US group, which differed significantly from the inhibition observed in the CIP and CIP+US groups. This finding may be related to the enhanced permeability of nanoparticles through biofilms. The inhibitory effect of the CPN+US group on bacterial biofilm activity was significantly increased by 51%, indicating that ultrasonic cavitation resulting from the liquid-gas phase change damaged the biofilm, thus enhancing biofilm penetration by the nanoparticles. The TCPN+US group showed the greatest inhibition on bacteria viability (93%), indicating that the TCPN+US group had the best inhibitory effect on biofilm activity.

Further *in vitro* evaluations of antibacterial performance were undertaken by measurement of the bacterial CFUs following treatment in each group (**Figure 3C**). Compared to the control group, there were no significant alterations in the number of colonies in the CIP and CIP+US groups,

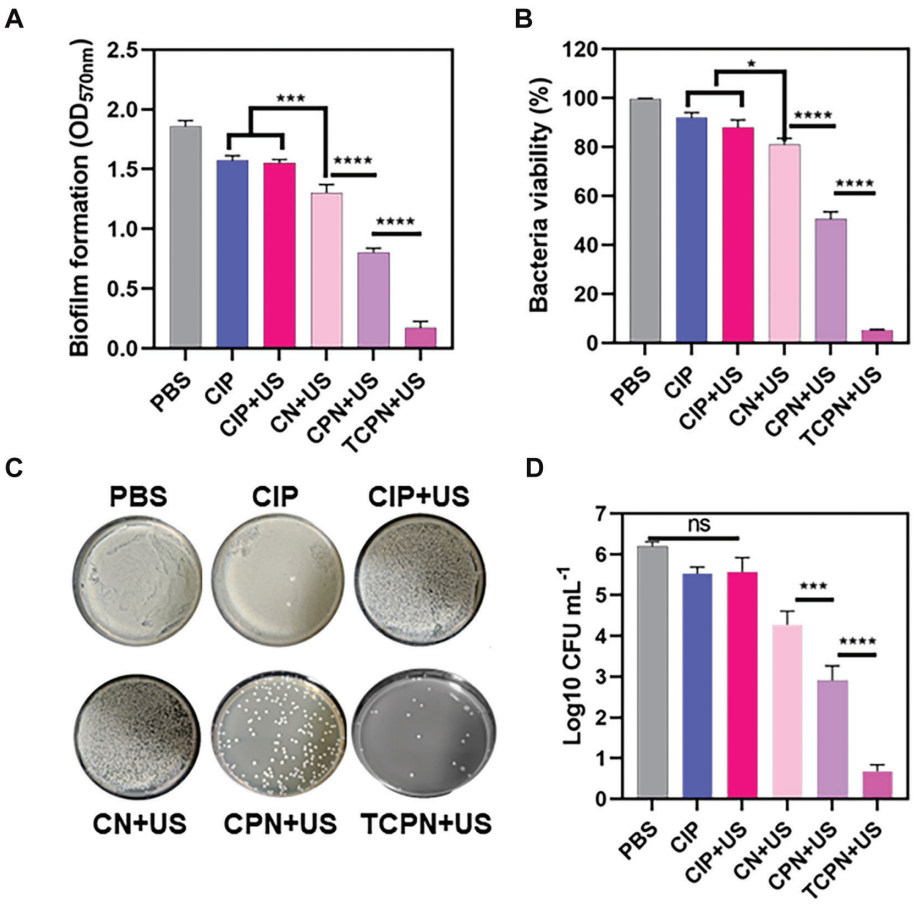

Figure 3 The bactericidal efficacy of TCPN nanoparticles *in vitro*. Biofilms were evaluated in terms of A) biomass using crystal violet staining, B) viability of bacteria using XTT assays, and C, D) CFUs by colony counting. The US parameters were as follows: intensity, 1.5 W cm^{-2}; frequency, 1 MHz; duty cycle, 50%; and duration, 10 min. Data are represented as the mean ± SD (n = 3) and analyzed by one-way ANOVA. Statistical significance: **P*<0.05; ****P*<0.001, and *****P*<0.0001.

indicating that the drugs alone or US-treated drugs did not have antibacterial properties. However, the CPN+US groups showed significant decreases in the number of *P. aeruginosa* colonies, which was attributed to the ultrasonic cavitation resulting from the liquid-gas phase changes, damaging the biofilm, and improving penetration of the nanoparticles. In the TCPN+US group, there was almost no colony growth on agar after ultrasonic irradiation, indicating that TCPN+US had the strongest antibacterial effect.

The bactericidal rates were assessed using the plate colony counting method (**Figure 3D**). Bacterial killing was greatest in the TCPN+US group, with the strongest antibacterial activity, and a five order of magnitude decrease in the number of colonies, which was equivalent to a bactericidal rate >99%. The number of bacterial colonies in the CPN+US group decreased by three orders of magnitude, indicating lower antibacterial activity compared to the TCPN+US group, while the number of colonies in the CIP and CIP+US groups decreased by one order of magnitude. Due to the rapid proliferation of surviving bacteria, which led to reinfection, a reduction of one order of magnitude in the bacterial killing efficiency is not sufficient for true clinical antibacterial application.

Therefore, the above results demonstrated unequivocally that the TCPN+US group had good antibacterial performance against *P. aeruginosa*. The main mechanisms were that the anti-*P. aeruginosa* antibody enhanced nanoparticle targeting and the liquid-gas phase change in the nanoparticles enhanced the biofilm penetration of the antibiotic CIP, working together with the antibiotic to exert an acoustic dynamic effect under the action of ultrasound to produce ROS, thereby killing *P. aeruginosa* cells deep within the biofilm and thus clearing the biofilm.

In vitro evaluation of biofilm elimination

The effects of different treatments on biofilms were investigated using a bacterial live/dead staining kit and evaluated by CLSM. The survival of bacteria in the different groups is shown in **Figure 4A**, in which green fluorescence indicates live bacteria and red fluorescence indicates dead bacteria. Bacteria in the control, CIP, and CIP+US groups were almost all green, indicating that the biofilm was not damaged, while those in the CN+US and CPN+US groups showed an alternating red and green distribution, indicating varying degrees of damage to the biofilm. There was very little green fluorescence in the TCPN+US group, with most of the bacteria fluorescing red, indicative of dead cells and

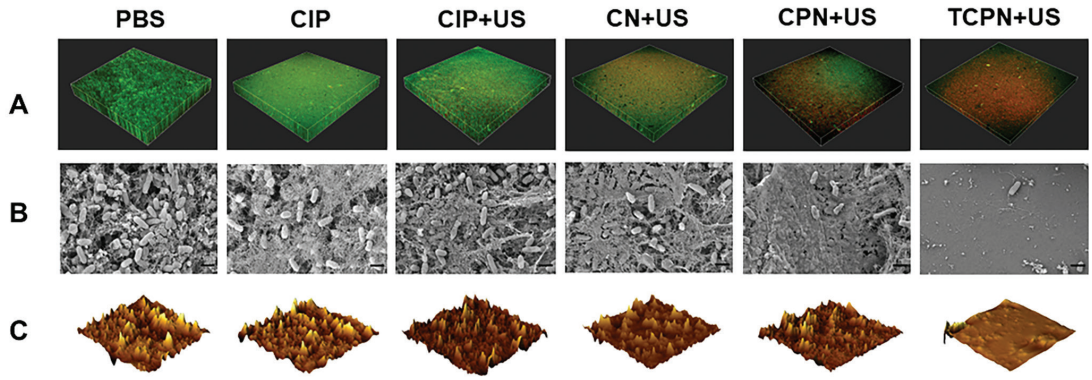

Figure 4 Elimination of biofilm *in vitro*. A) Live/dead staining of *Pseudomonas aeruginosa* biofilms in the PBS, CIP, CIP+US, CN+US, CPN+US, and TCPN+US groups (US parameters: 1.5 W cm^{-2} intensity; 50% duty cycle; 1 MHz frequency; and 10 min duration). Live bacteria were stained using SYTO 9 (green) and dead bacteria were stained using PI (red). Biofilm morphology shown by B) SEM, and C) AFM in the PBS, CIP, CIP+US, CN+US, CPN+US, and TCPN+US groups (US parameters were same as above).

biofilm destruction. The results showed that the TCPN+US group had the strongest biofilm clearance ability.

SEM was used for morphologic analysis of the biofilm. The SEM images showed remarkable changes in the biofilm of different treatment groups. **Figure 4B** shows the thick biofilm produced by *P. aeruginosa* in the control group. The bacteria in the control, CIP, and CIP+US groups aggregated to form dense biofilms. However, while the biofilm in the CN+US and CPN+US groups remained dense, the biofilms were different from the control group, with slightly reduced numbers of *P. aeruginosa*. There was no biofilm visible in the TCPN+US group, with only a small number of *P. aeruginosa* present, and the silicon wafers were exposed.

In addition, changes in biofilm morphology were also evaluated through AFM images. **Figure 4C** shows the 3D AFM images of the treated biofilms in the different groups. Breakage of the biofilm into smaller and thinner pieces was visible in the TCPN+US group. A comparison of the average surface roughness (**Figure S1**) showed that this was reduced most significantly in the TCPN+US group, which confirmed the reduction in biofilm biomass after treatment in the TCPN+US group. Both the SEM and AFM results verified the effectiveness of TCPN+US treatment for biofilm removal, confirming the findings of the crystal violet staining and XTT experiment.

Evaluation of penetration and membrane permeability

Most treatments cannot remove biofilms because the extracellular polymers produced by the bacteria prevent the penetration of bactericides into the biofilm. Therefore, the penetrative ability of nanomaterials is crucial for biofilm elimination. To investigate this, SYTO 9 dye was used to label *P. aeruginosa* biofilm and DiI was used to label the CN, CPN, and TCPN nanoparticles. Then, the ability of the nanoparticles to penetrate the biofilm was evaluated using CLSM. As shown in **Figure 5A**, significant differences in the fluorescence distribution between the CN+US, CPN+US, and TCPN+US groups were observed. While the CN+US and CPN+US groups showed no significant red fluorescence, there was a uniform distribution of red fluorescence throughout the entire biofilm in the TCPN+US group. Quantitative analysis of fluorescence (**Figure 5B**) confirmed the penetration ability of TCPN in the TCPN+US group, with red fluorescence in the TCPN+US group being six times higher than the control group ($P<0.0001$). This finding indicated that TCPN penetrated the biofilm efficiently, resulting in the delivery of the antibiotic to the deep of the biofilm, which was combined with an acoustic dynamic effect and made it easier to kill bacteria in the biofilm.

To further investigate the effect of TCPN+US on *P. aeruginosa*, separate NPN and ONPG analyses were performed, which reflected the membrane permeability level. It was found (**Figure 5C**) that the NPN fluorescence intensity increased significantly over time in the positive control group, with similar results in the TCPN+US treatment group, and low fluorescence intensity occurred in the negative control group. This finding indicated that TCPN+US damaged the outer membrane of *P. aeruginosa*. ONPG analysis reflected the permeability of the bacterial inner membrane and **Figure 5D** showed greater permeability of the inner membrane in the TCPN+US treatment group compared with the positive controls. These findings demonstrated that TCPN+US caused damage to the inner membrane of *P. aeruginosa*, which was beneficial for ROS to enter the bacteria and disrupt its metabolism, leading to bacterial death.

In vivo wound healing evaluation of TCPN

Mice were euthanized at various time points after infection. Tissues of the infected wounds were collected and the formation of biofilm in the wounds was confirmed using SEM, H&E staining, and Masson staining. As indicated in **Figure S2**, SEM showed that 24 h after infection small amounts of EPSs and biofilms were observed in the wound tissues, while after 48 h large amounts of EPSs and biofilms were present with the bacteria wrapped in the biofilms. Both H&E and Masson staining showed that a small amount of

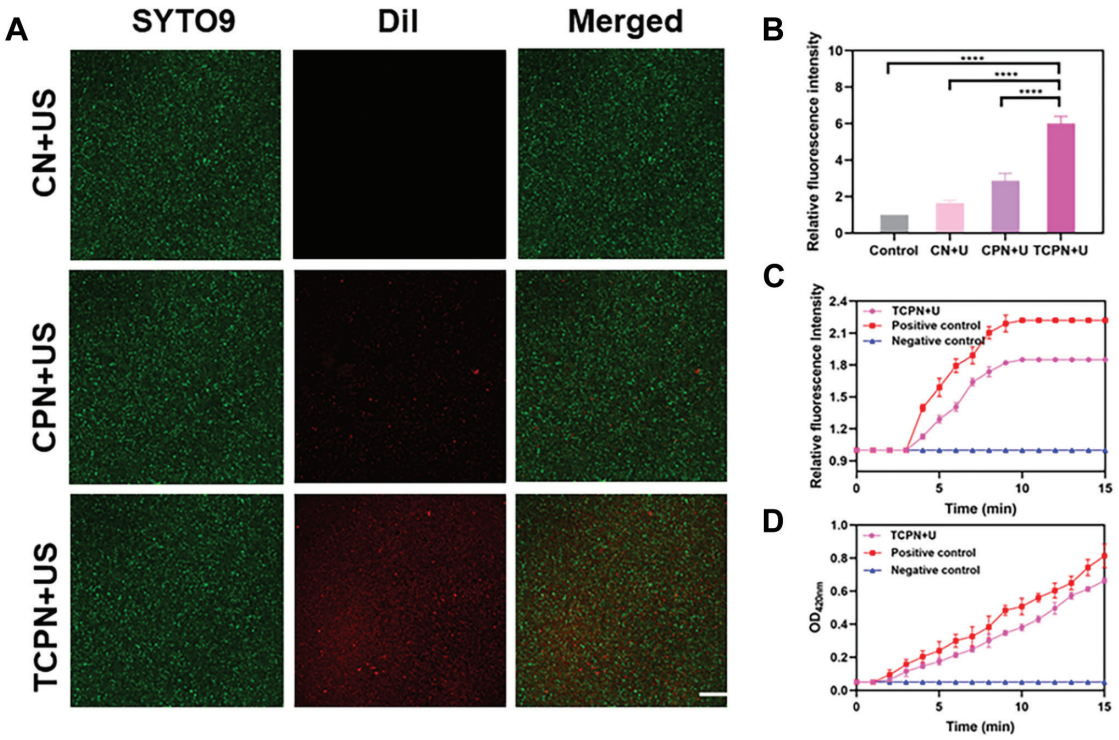

Figure 5 Penetration ability assessment. A) CLSM images of *Pseudomonas aeruginosa* biofilm after treatment with CN+US, CPN+US, and TCPN+US. US parameters were as follows: 1.5 W cm^{-2} intensity; 50% duty cycle; 1 MHz frequency; and 10 min duration. Green fluorescence indicated staining of *P. aeruginosa* with SYTO 9, while red fluorescence indicated DiI in nanoparticles. Scale bar = 100 μm. B) Quantification of fluorescence in A). C) Permeability of the outer membrane was assessed by NPN fluorescence after treatment with TCPN under US (US parameters as above). D) Permeability of the inner membrane of bacteria was measured by ONPG after treatment with TCPN under US (US parameters as above). Data are represented as the mean ± SD and analyzed by one-way ANOVA. Statistical significance: ****P<0.0001.

inflammatory cell infiltration in the wounds after 24 h, which increased markedly after 48 h, indicating the formation of biofilms in the infected wounds after 48 h.

Figure 6A shows a schematic diagram of the experimental model and treatments used. **Figure 6B** illustrates representative images of the wounds in the different groups on days 0, 2, 5, 8, and 11 after biofilm formation in the infected wounds. On the 11th day the wounds in the TCPN group had healed. Due to the formation of biofilms, even on the 11th day after injury the wounds in the other treatment groups were not completely healed. Wound healing was further evaluated in detail, as shown in **Figure 6C-E**. The wounds treated with TCPN+US contracted faster, with a reduction of nearly 50% in the wound area in the first 5 days and approximately 90% in the 8 days after treatment (**Figure 6D**). We further explored the efficacy of the TCPN+US group in killing *P. aeruginosa* in wound biofilms by detecting the bacterial load in infected wounds. The number of bacteria in the wound sites was investigated 3 d after infection (**Figure 6E**). Relative to high bacterial survival rates in the control and other treatment groups, the bacterial survival rate in the TCPN+US group was approximately 10%. Therefore, TCPN+US not only achieved significant antibacterial effects against *P. aeruginosa in vitro* but was also found to have excellent antibacterial effects against *P. aeruginosa* in infected wound biofilms *in vivo*. Histologic analysis of the wound tissues using H&E staining on day 12 after biofilm formation (**Figure 6C**) showed that there was still infiltration of inflammatory cells in wounds from the treatment groups that did not receive TCPN treatment, while the TCPN+US group showed complete re-epithelialization, similar to normal skin tissue and normal hair follicle structure was regenerated. These results indicate that TCPN contributes to wound healing.

Cell migration is fundamental for angiogenesis and fibrogenesis, and is of great importance for wound healing. Cell migration was evaluated using *in vitro* scratch tests. As shown in **Figure S3**, the HUVECs in each group were initially scratched by the same width (0 h). After 24 h of culture, the cell gap between the scratches had decreased in all study groups, indicating cell migration. Compared to cells under other treatments, cells treated with TCPN+US exhibited greater migration ability with significantly narrower gaps. This result indicated that TCPN promotes cell migration to wounds. It is also consistent with the *in vivo* experimental results of TCPN+US, which is beneficial for wound healing.

Biocompatibility of TCPN

For any antibacterial drug designed for therapeutic purposes, biocompatibility is an important issue. Anti-biofilm drugs should have good antibacterial effects and the ability to clear biofilm, together with minimal toxicity and overall systemic safety. Thus, the potential hemolysis of RBCs by TCPN was investigated, which showed that TCPN and the other groups had good blood compatibility, with hemolysis rates <5%, indicating no significant damage to RBCs (**Figure 7A**). The potential cytotoxicity of TCPN was then investigated. After

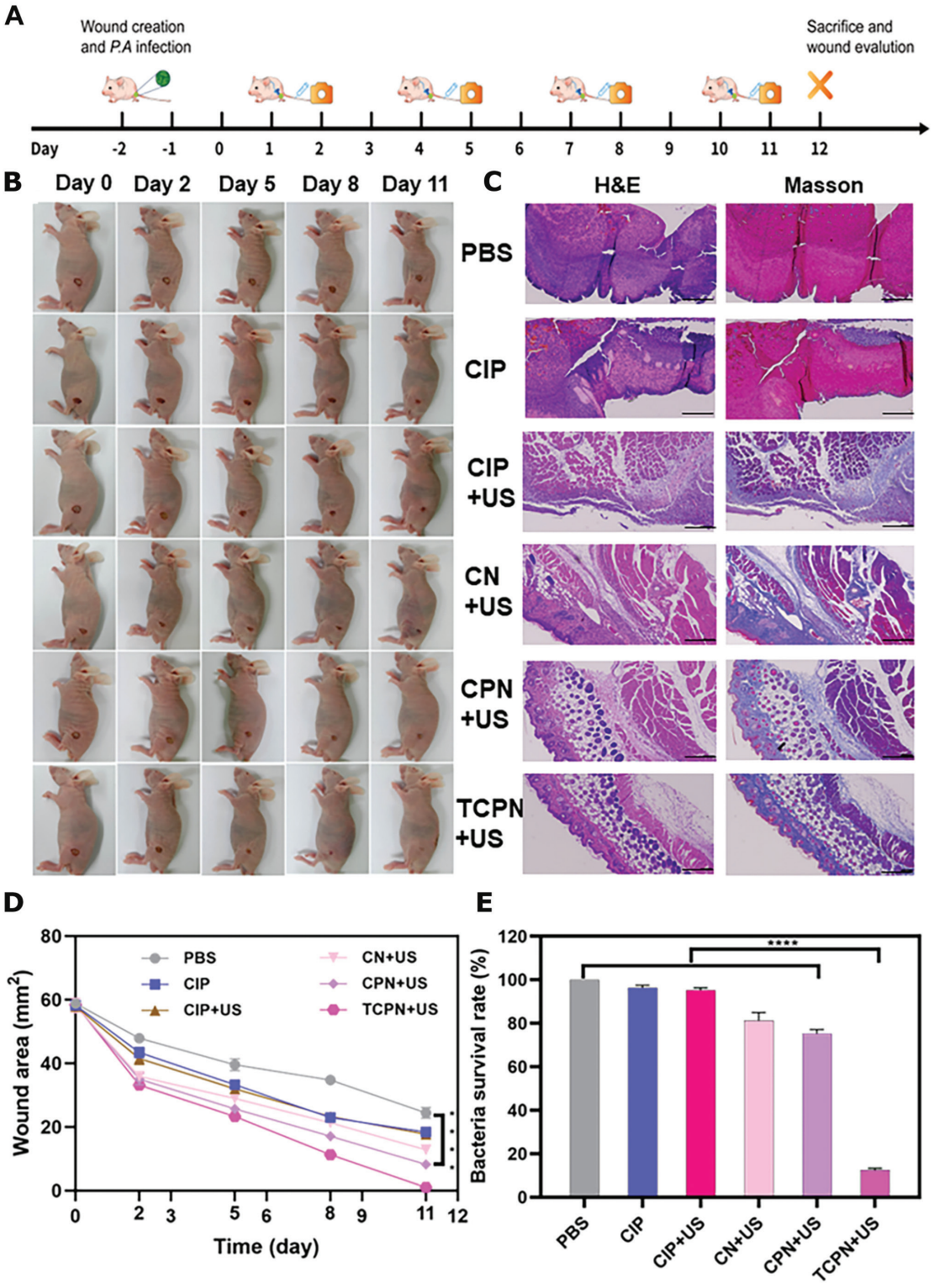

Figure 6 Antibacterial effects and wound healing *in vivo*. A) Schematic diagram of the experimental model and treatments. B) Images of wounds infected with *Pseudomonas aeruginosa* after treatment with PBS, CIP, CIP+US, CN+US, CPN+US, and TCPN+US (US parameters: 1.5 W cm^{-2} intensity; 50% duty cycle; 1 MHz frequency; and 10 min duration) on days 0, 2, 5, 8, and 11. C) H&E and Masson staining of wound tissues on day 12. Scale bar = 200 μm. D) Quantification of wound areas after 3 days of different treatments. E) Bacterial survival rates at day 12. Data are presented as the mean ± SD (n = 6) and analyzed by 2-way ANOVA. Statistical significance: ****P<0.0001.

treating HUVECs and NIH/3T3 cells with TCPN, cytotoxicity was analyzed using the CCK-8 assay. As illustrated in **Figure 7B**, there was no significant alteration in cell viability in any of the groups, with viability remaining >85%, indicating that TCPN is biocompatible with cells. Finally, the systemic toxicity of TCPN to major organs was evaluated through *in vivo* serum biochemical testing and H&E staining of organ tissues. As illustrated in **Figure 7C**, no significant differences were detected in blood biochemical indicators, including RBCs, WBCs, PLTs, and ALT, AST, ALP, BUN, and CR levels compared to the control group. This finding indicated that TCPN has no toxicity in mice. In addition,

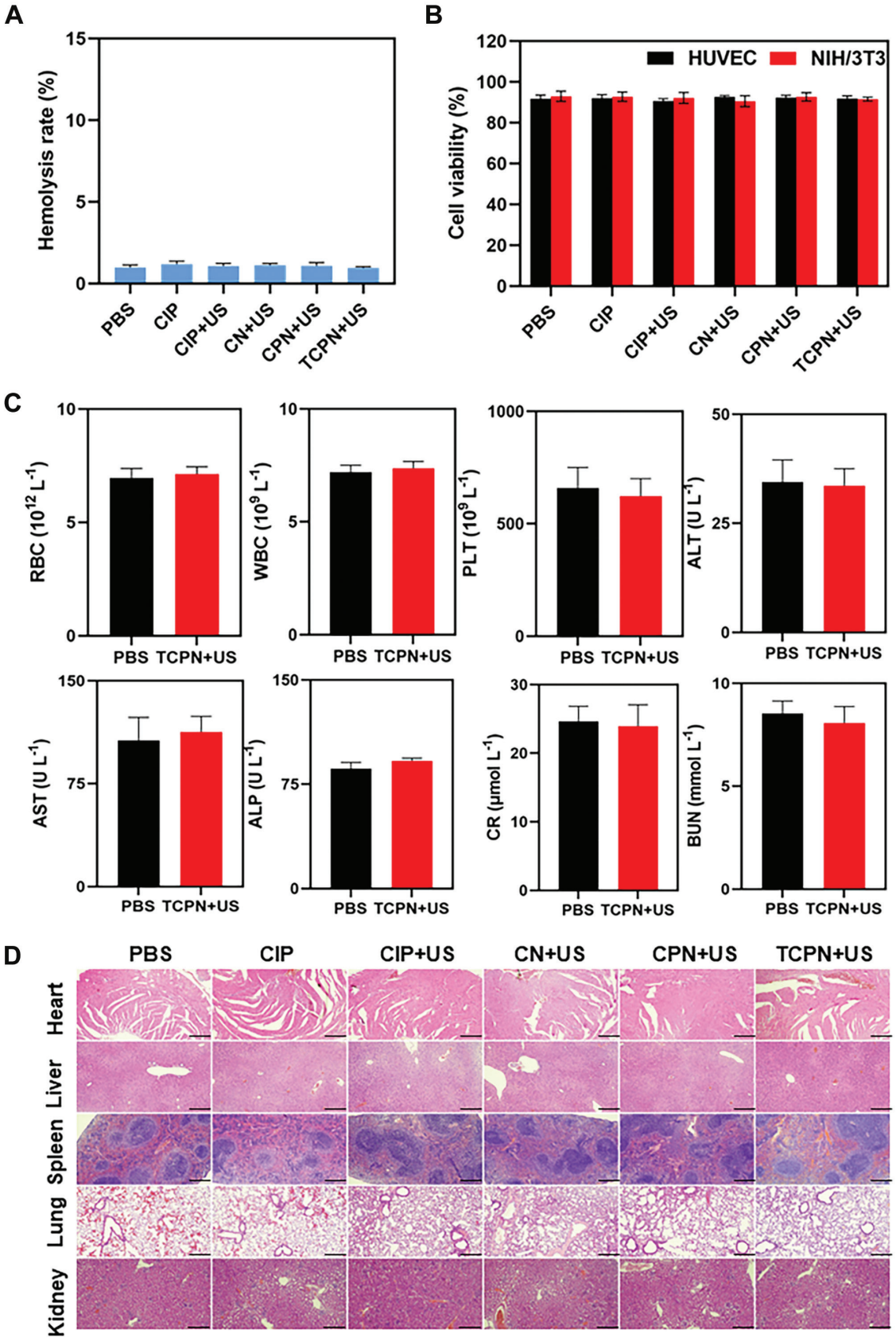

Figure 7 Biosafety and biocompatibility of TCPN. A) Assessment of hemolysis after different treatments. B) Cell viability of HUVECs and NIH/3T3 cells after different treatments. C) Blood routine test and biochemical indicators in mice 12 days after treatment with TCPN. D) H&E staining of tissues from the organs after treatment in the different groups, scale bar = 200 μm.

H&E histologic analysis of heart, liver, lung, spleen, and kidney sections showed no evidence of damage or inflammation after 14 d of treatment (**Figure 7D**). Therefore, TCPN is both biocompatible and safe, suggesting the potential application for removal of biofilms.

Conclusion

In summary, we developed a novel ultrasound-launched targeted nanoparticle, TCPN, composed of a PLGA polymer loading CIP and PFP. TCPN was shown to be effective for delivery of antibiotics, killing of bacteria, and removal of biofilms via enhanced penetration of the biofilm and targeting of the antibiotics. The nanoparticle showed a sensitive response to ultrasonic stimulation, including rapid liquid-gas phase transition, cavitation effect, and biofilm destruction to allow deep penetration of the antibiotics. In addition, the bacteria-specific antibody was conjugated on the nanoparticle to target and bind to bacteria. Under US irradiation, CIP generated ROS in the bacterial cells, leading to bacteria death. Therefore, the TCPN nanoparticle represents a promising approach to manage antibiotic resistance and the removal of biofilms via ultrasonic cavitation and antibacterial SDT.

Experimental section

Materials

PLGA–COOH (50:50, MW = 12.0 kDa) was obtained from Jinan Daigang Biomaterial Co. (Shandong, China). PFP was obtained from J&K Scientific (Beijing, China), and dichloromethane (DCM), polyvinyl alcohol (PVA), 1-(3-dimethylaminopropyl)-3-ethylcarbodiimide hydrochloride (EDC), N-hydroxysuccinimide (NHS), MES buffer, the fluorescent dye, DiI, and CIP were obtained from Sigma-Aldrich (St. Louis, MO, USA). The LIVE/DEAD™ BacLight™ Bacterial Viability Kit, XTT Proliferation Assay Kit, the anti-*P. aeruginosa* antibody (Thermo Fisher Scientific MA1-83430, B11), and FITC-conjugated secondary antibody were obtained from Invitrogen (Thermo Fisher Scientific, Waltham, MA, USA), while DCFH-DA working fluid was from Biyuntian (Shanghai, China). Deionized water (DI, Millipore Milli-Q grade) was used throughout. All other reagents and solvents were of analytical grade and were used with no additional purification.

Preparation of TCPN nanoparticles

The TCPN containing the liposoluble antibiotic CIP was prepared as an oil-in-water single-emulsion by solvent evaporation. PLGA (100 mg), CIP (10 mg), and PFP (50 μL) were dissolved in a DCM organic phase (6 mL) before mixing and emulsification with an aqueous solution of PVA using sonication (output power, 60 W; intensity, 80%; duration, 5 min) with a sonicator microtip probe (Bandelin Sonopuls, Berlin, Germany) on ice. The organic phase was allowed to evaporate by stirring at room temperature overnight on a magnetic stirrer. The nanoparticles were collected by centrifugation at 10,000 rpm, followed by thrice-washing in distilled water and designated as CPN. The preparation of CN nanoparticles was performed in the same way but without PFP. Anti-*P. aeruginosa* antibodies were coupled to the CPN nanoparticles by carbodiimide conjugation. Briefly, the CPN nanoparticles (1 mg) were placed in 10 mL of 0.1 M 2-(N-morpholino)ethanesulfonic acid [MES; pH 5.5, containing 6 mg of 1-ethyl-3-(3-dimethylaminopropyl) carbodiimide [EDC] and 20 mg of N-hydroxysuccinimide [NHS]), and allowed to react for 30 min with gentle shaking. After centrifugation and thrice-washing in distilled water for removal of unreacted EDC and NHS, the precipitate was redissolved in 10 mL of 0.1 M MES (pH 8.0). An excess of the anti-*P. aeruginosa* antibody (B11) as added and incubated with gentle shaking for 90 min. After centrifugation at 10,000 rpm and thrice-washing of the precipitate with distilled water for removal of unconjugated antibody, the TCPN nanoparticles were stored at 4°C until use. These procedures were all performed on ice.

TCPN characterization

The morphology of the TCPN nanoparticles was evaluated by scanning electron microscopy ([SEM] S-4800N; Hitachi, Tokyo, Japan), while the shapes were assessed by transmission electron microscopy ([TEM] H-7700; Hitachi) after negative staining with 2% (w/v) sodium phosphotungstate. The mean diameters, polydispersity index (PDI), and zeta potentials were examined with a dynamic light scattering analyzer ([DLS], Zetasizer Nano-ZS; Malvern Instruments, Malvern, UK). To ensure the stability of the nanoparticles, DLS measurements were obtained within 21 days.

Assessment of drug-loading and encapsulation efficiencies

Ultraviolet spectrophotometry was used to determine the loading efficiency (LE) and encapsulation efficiency (EE) of CIP, with calculations according to the standard concentration curve of CIP using the following equations:

$$LE=\frac{W_1}{W_2}\times 100\% \quad (1)$$

$$EE=\frac{W_1}{W_3}\times 100\% \quad (2)$$

where W_1 is the concentration of the drug that was loaded, W_2 represents the total concentration of drug and carrier, and W_3 is the original drug concentration.

Assessment of antibody-TCPN conjugation

To assess antibody-TCPN conjugation, DiI-labeled TCPN was probed with an FITC-conjugated secondary antibody

for 2 h in an ice bath with gentle shaking. The bound fluorescence was assessed under a confocal laser-scanning microscope ([CLSM] TCS Sp5; Leica, Wetzlar, Germany) and the degree of conjugation was calculated. Circular dichroism (CD) spectra were acquired on a CD spectrometer (Chirascan V100; Applied Photophysics, Surrey, UK) using 1-mm pathlength quartz cuvettes (Hellma 110-QS; Applied Photophysics). Fourier-transform infrared (FTIR) spectra were acquired on an FTIR spectrometer (Nicolet 5700; Thermo Nicolet Corporation, Madison, WI, USA).

Bacterial biofilm formation and harvesting

Bacterial strains were purchased from the American Type Culture Collection (ATCC, Manassas, VA, USA). *P. aeruginosa* (ATCC 27853) was used as a representative biofilm-forming bacterium in this study. Single colonies of *P. aeruginosa* were inoculated in LB broth and cultured overnight at 37°C on a shaker (220 rpm), after which 100 µL of the bacterial suspension was added to 10 mL of fresh medium and grown for another 4 h until reaching mid-log-phase growth. The optical density (OD)600 values were assessed and the bacteria were then placed in 96-well plates and allowed to grow for 48 h at 37°C with replacement of the medium after 24 h. After removal of the media, the biofilm on the plates was washed with PBS and used for further experiments.

XTT assays and crystal violet (CV) staining

XTT assays were used to assess biofilm growth. After rinsing the wells containing biofilm with PBS, 100 µL of XTT solution were placed in each well and reacted for 1 h at 37°C in the dark. Formazan color formation was evaluated at 450 nm in a microplate reader, indicating the metabolic activity associated with biofilm growth. The biomass of the biofilms was examined by CV staining. After air-drying for 30 min or until completely dried, the biofilms were fixed in methanol for 15 min, after which the biofilms were once again air-dried, followed by staining with CV (0.2% [w/v]) for 10 min and gentle rinsing with two changes of PBS. Ethanol was used to re-solubilize the stain within the biofilm and the absorbances at 570 nm were assessed with the microplate reader.

Counting of colonies in the biofilm

Biofilms in 96-well plates were incubated with different treatments. An acoustic intensity of 1.5 W cm^{-2} was used together with a 50% duty cycle and a frequency of 1 MHz. After careful aspiration of excess liquid and thrice-washing with PBS, the bacterial cells were extracted from the biofilm using vigorous sonication for 10 min and crashing for 2 min. Following 10-fold serial dilutions, 100-µL aliquots of the final suspensions were spread evenly on agar and allowed to grow for 24 h at 37°C. Colony-forming units (CFUs) were counted and imaged using a digital camera.

Detection of ROS generation

ROS were measured using DCFH-DA. The biofilm-containing wells in the 96-well plates were divided into the PBS, CIP, CIP+US, and TCPN+US groups with 3 wells per group. Using CIP at a dosage of 0.1 mg mL^{-1}, 10 µM DCFH-DA working fluid (Biyuntian, S0033S, China) was added to each well. The US parameters were an intensity of 1.5 W cm^{-2}, duty cycle of 50%, frequency of 1 MHz, and duration time of 10 min. Following treatment, the wells were rinsed gently to remove residual nanoparticles and DCFH-DA, and fluorescence was evaluated and imaged using CLSM.

Live/dead staining

The viability of bacteria in biofilms was assessed by live/dead staining. Samples were treated with a SYTO 9-PI combination (30 min at room temperature in the dark). After thrice-washing in PBS, the biofilms were evaluated under CLSM.

Biofilm morphology

Biofilm morphology was assessed by SEM. Biofilms were generated on silicon wafers and fixed with 2.5% glutaraldehyde for 12 h at 4°C. Following dehydration in an ethanol gradient (incubation for 15 min each with 20%, 40%, 60%, 80%, and 100% ethanol) and platinum coating, the biofilms were evaluated by SEM.

Biofilm visualization by atomic force microscopy (AFM)

AFM was used to examine and image the morphologic characteristics of treated and untreated biofilms on glass surfaces. AFM micrographs were generated in tapping mode with the probe, examining biofilms grown in grease-free sterile coverslips in 6-well plates. After washing in sterile PBS, glutaraldehyde fixation, and ethanol dehydration, the coverslips were vacuum-dried. Gwyddion software was used to evaluate details of the surface topography.

Biofilm penetration

Penetration of biofilms by the nanoparticles was examined by CLSM. Briefly, DiI-labeled TCPN were treated with US and cultured with biofilms in 96-well plates for 10 min. After washing in PBS, the biofilms were then treated with SYTO 9 for 20 min in the dark, followed by further rinsing and evaluation of fluorescence under CLSM, with live bacteria stained green and DiI emitting red fluorescence.

Assay of membrane permeability

Membrane permeability was investigated using 1-N-phenylnaphthylamine (NPN) staining and quantification of NPN uptake by the cytoplasmic membranes of the bacteria. After overnight growth in LB, bacteria were diluted in PBS to an OD600 of 0.5, centrifuged twice at 4000 rpm for 10 min at 25°C, and resuspended in PBS. One hundred microliters of the suspension were then placed in each well of black 96-well plates, and after the addition of 50 μL of freshly prepared NPN (40 μM in 8% [v/v] acetone), reacted at room temperature for 30 min. After addition of US-treated TCPN, fluorescence was read immediately in a plate reader, with excitation and emission wavelengths of 350 and 420 nm, respectively. The amount of dye taken up was determined by subtraction of free NPN (baseline) from the total measured fluorescence and expressed as relative fluorescence units. Permeabilization of the inner membrane of the bacteria was assessed using O-nitrobenzene-β-D-galactopyranoside (ONPG) as a substrate for β-galactosidase secreted from the bacterial cytoplasm. Bacterial suspensions (1.6 mL) in 0.5% NaCl (pH 6.8-7.3 after adjustment with 1.0 M phosphate buffer) were incubated with 150 μL of 30 mM ONPG. After US treatment of TCPN, the production of o-nitrophenol was monitored by the absorption value at 420 nm. Experiments were performed in triplicate.

Establishment of mouse models with subcutaneous Pseudomonas aeruginosa infection

BALB/c nude mice (male, 15–20 g) were obtained from the Laboratory Animal Center of Zhejiang Academy of Medical Sciences. All animal studies were performed in compliance with the guidelines and ethical standards approved by the Ethics Committee of Zhejiang Academy of Medical Sciences (No. IACUC-20200222-03). Subcutaneous infections were performed by creating a 9-mm diameter full-thickness skin wound on the right leg upon which a *P. aeruginosa* suspension (10^9 CFU mL^{-1}) was spread. The infection was established after 48 h.

Cell scratch test

HUVEC cells were cultured in RPMI-1640. Cells were seeded at 4×10^5/well in 6-well plates and grown to a monolayer overnight. A straight scratch was made in the monolayer using a 200-μL pipette tip, followed by gentle washing with PBS to remove debris. Cells were divided into six groups (PBS, CIP, CIP+US, CN+US, CPN+US, and TCPN+US) with three wells per group. The dosage was 0.1 mg mL^{-1}, calculated by CIP, and the ultrasonic parameters were 1.5 W cm^{-2}, a duty cycle of 50%, a frequency of 1 MHz, and a treatment time of 10 min. After 24 h, the cells were imaged under a microscope.

Cytotoxicity test

Mouse NIH/3T3 fibroblasts or HUVECs were inoculated in 96-well plates (5×10^3 cells/well) and grown in DMEM and RPMI-1640, respectively, in a humidified incubator for 24 h with 5% CO_2 at 37°C. Following different treatments of the groups, 20 μL of CCK-8 reagent was placed in each well and incubated for 2 h. Absorbances at 450 nm were measured to assess the viability of the cells.

Hemolysis test

Hemolysis was determined to evaluate blood compatibility. First, anticoagulated venous blood was centrifuged at 8000 rpm for 5 min, followed by thrice-washing with 0.9% NaCl and resuspension of the red blood cells (RBCs) in 0.9% NaCl. Fifty microliter aliquots of this suspension were then treated according to the group allocations using 0.9% NaCl and ultra-pure water as negative and positive controls, respectively. The suspensions were incubated at 37°C for 1 h, followed by centrifugation at 6000 rpm for 5 min and measurement of absorbance of the supernatant at 540 nm for calculation of hemolysis as follows:

$$\text{Hemolysis rate (\%)}=\frac{(A-AN)}{(AP-AN)}\times100\% \quad (3)$$

where A, AN, and AP indicate the absorbance of RBCs exposed to different treatment, 0.9% NaCl solution (negative control), and ultra-pure water (positive control), respectively.

Blood biochemical analysis

TCPN was administered intravenously to healthy mice. Twelve days after injection, blood was obtained from the retro-orbital sinus, centrifuged, and analyzed using an automatic biochemical analyzer (Model 7170; Hitachi). The measurements included white blood cell (WBC), RBC, and platelet (PLT) counts, as well as liver and kidney markers, such as ALT, AST, ALP, CR, and BUN.

Histologic analysis

Twelve days after infection, the mice were sacrificed, and the subcutaneous abscesses were collected, fixed in 4% paraformaldehyde, embedded in paraffin, and sectioned. The sections were stained with hematoxylin and eosin (H&E) and Masson stains before evaluation under an optical microscope.

Statistical analysis

All experiments were performed a minimum of three times. The data are presented as the mean ± standard deviation (SD) and were analyzed using GraphPad Prism 9 (GraphPad

Software, San Diego, CA, USA) using one-way ANOVA or Student's t-tests. The levels of significance were as follows: *P<0.05; **P<0.01; ***P<0.001; and ****P<0.0001.

Supporting information

Supporting information is available from the Wiley Online Library or from the author.

Acknowledgements

X.L., J.S., and Z.H. contributed equally to this work. This study was financially supported by the National Natural Science Foundation of China (Grant Nos. 82030048, 82230069, 82371967, 82102191, and 82001818) and the Key Research and Development Program of Zhejiang Province (Grant No. 2019C03077). The authors acknowledge Lulu Jin, Yingying Zhang, and Xi Zheng for their technical assistance in designing and performing the experiments.

Conflict of interest

The authors declare no conflicts of interest.

Data availability statement

The data that support the findings of this study are available from the corresponding author upon reasonable request.

References

[1] Dong Y, Wang L, Yuan K, Ji F, Gao J, et al. Magnetic microswarm composed of porous nanocatalysts for targeted elimination of biofilm occlusion. ACS Nano 2021;15:5056. [PMID: 33634695 DOI: 10.1021/acsnano.0c10010]

[2] Behlau I, Gilmore MS. Microbial biofilms in ophthalmology and infectious disease. Arch Ophthalmol 2008;126:1572-81. [PMID: 19001227 DOI: 10.1001/archopht.126.11.1572]

[3] Liu Y, Shi L, Su L, van der Mei HC, Jutte PC, et al. Nanotechnology-based antimicrobials and delivery systems for biofilm-infection control. Chem Soc Rev 2019;48:428. [PMID: 30601473 DOI: 10.1039/c7cs00807d]

[4] Koehbach J, Gani J, Hilpert K, Craik DJ. Comparison of a short linear antimicrobial peptide with its disulfide-cyclized and cyclotide-grafted variants against clinically relevant pathogens. Microorganisms 2021;9:1249. [PMID: 34201398 DOI: 10.3390/microorganisms9061249]

[5] Pendleton JN, Gorman SP, Gilmore BF. Clinical relevance of the ESKAPE pathogens. Expert Rev Anti Infect Ther 2013;11:297-308. [PMID: 23458769 DOI: 10.1586/eri.13.12]

[6] Ghafoor A, Hay ID, Rehm BH. Role of exopolysaccharides in Pseudomonas aeruginosa biofilm formation and architecture. Appl Environ Microbiol 2011;77:5238-46. [PMID: 21666010 DOI: 10.1128/AEM.00637-11]

[7] Martinez SR, Ibarra LE, Ponzio RA, Forcone MV, Wendel AB, et al. Photodynamic Inactivation of ESKAPE Group bacterial pathogens in planktonic and biofilm cultures using metallated porphyrin-doped conjugated polymer nanoparticles. ACS Infect Dis 2020;6:2202. [PMID: 32538610 DOI: 10.1021/acsinfecdis.0c00268]

[8] Flemming HC, Wingender J, Szewzyk U, Steinberg P, Rice SA, et al. Biofilms: an emergent form of bacterial life. Nat Rev Microbiol 2016;14:563. [PMID: 27510863 DOI: 10.1038/nrmicro.2016.94]

[9] Peterson BW, He Y, Ren Y, Zerdoum A, Libera MR, et al. Viscoelasticity of biofilms and their recalcitrance to mechanical and chemical challenges. FEMS Microbiol Rev 2015;39:234-45. [PMID: 25725015 DOI: 10.1093/femsre/fuu008]

[10] Pogodin S, Hasan J, Baulin VA, Webb HK, Truong VK, et al. Biophysical model of bacterial cell interactions with nanopatterned cicada wing surfaces. Biophys J 2013;104:835-40. [PMID: 23442962 DOI: 10.1016/j.bpj.2012.12.046]

[11] Chung KK, Schumacher JF, Sampson EM, Burne RA, Antonelli PJ, et al. Impact of engineered surface microtopography on biofilm formation of Staphylococcus aureus. Biointerphases 2007;2:89-94. [PMID: 20408641 DOI: 10.1116/1.2751405]

[12] Banerjee I, Pangule RC, Kane RS. Antifouling coatings: recent developments in the design of surfaces that prevent fouling by proteins, bacteria, and marine organisms. Adv Mater 2011;23:690-718. [PMID: 20886559 DOI: 10.1002/adma.201001215]

[13] Kalicke T, Schierholz J, Schlegel U, Frangen TM, Koller M, et al. Effect on infection resistance of a local antiseptic and antibiotic coating on osteosynthesis implants: an in vitro and in vivo study. J Orthop Res. 2006;24:1622. [PMID: 16779814 DOI: 10.1002/jor.20193]

[14] Kennedy JE. High-intensity focused ultrasound in the treatment of solid tumours. Nat Rev Cancer 2005;5:321-7. [PMID: 15776004 DOI: 10.1038/nrc1591]

[15] Guan W, Tan L, Liu X, Cui Z, Zheng Y, et al. Ultrasonic interfacial engineering of red phosphorous-metal for eradicating MRSA infection effectively. Adv Mater 2021;33:e2006047. [PMID: 33349987 DOI: 10.1002/adma.202006047]

[16] Qian X, Han X, Chen Y. Insights into the unique functionality of inorganic micro/nanoparticles for versatile ultrasound theranostics. Biomaterials 2017;142:13. [PMID: 28719818 DOI: 10.1016/j.biomaterials.2017.07.016]

[17] Ahmed HU, El-Shater Bosaily A, Brown LC, Gabe R, Kaplan R, et al. PROMIS Study Group. Diagnostic accuracy of multi-parametric MRI and TRUS biopsy in prostate cancer (PROMIS): a paired validating confirmatory study. Lancet 2017;389:815-22. [PMID: 28110982 DOI: 10.1016/S0140-6736(16)32401-1]

[18] Su K, Tan L, Liu X, Cui Z, Zheng Y, et al. Rapid photo-sonotherapy for clinical treatment of bacterial infected bone implants by creating oxygen deficiency using sulfur doping. ACS Nano 2020;14:2077. [PMID: 31990179 DOI: 10.1021/acsnano.9b08686]

[19] Han X, Huang J, Jing X, Yang D, Lin H, et al. Oxygen-deficient black titania for synergistic/enhanced sonodynamic and photoinduced cancer therapy at near infrared-ii biowindow. ACS Nano 2018;12:4545. [PMID: 29697960 DOI: 10.1021/acsnano.8b00899]

[20] Wang D, Cheng DB, Ji L, Niu LJ, Zhang XH, et al. Precise magnetic resonance imaging-guided sonodynamic therapy for drug-resistant bacterial deep infection. Biomaterials 2021;264:120386. [PMID: 32979656 DOI: 10.1016/j.biomaterials.2020.120386]

[21] Pang X, Liu X, Cheng Y, Zhang C, Ren E. Sono-immunotherapeutic nanocapturer to combat multidrug-resistant bacterial infections. Adv Mater 2019;31:e1902530. [PMID: 31222947 DOI: 10.1002/adma.201902530]

[22] Pang X, Xiao Q, Cheng Y, Ren E, Lian L, et al. Bacteria-responsive nanoliposomes as smart sonotheranostics for multidrug

resistant bacterial infections. ACS Nano 2019;13:2427-2438. [PMID: 30657302 DOI: 10.1021/acsnano.8b09336]

[23] Huang B, Wang L, Tang K, Chen S, Xu Y, et al. IR780 Based sonotherapeutic nanoparticles to combat multidrug-resistant bacterial infections. Front Chem 2022;10:840598. [PMID: 35141201 DOI: 10.3389/fchem.2022.840598]

[24] Serpe L, Giuntini F. Sonodynamic antimicrobial chemotherapy: First steps towards a sound approach for microbe inactivation. J Photochem Photobiol B 2015;150:44-9. [PMID: 26037696 DOI: 10.1016/j.jphotobiol.2015.05.012]

[25] Liu B, Wang DJ, Wang X, Liu BM, Kong YM, et al. Spectroscopic investigation on protein damage by ciprofloxacin under ultrasonic irradiation. Spectrochim Acta A Mol Biomol Spectrosc 2011;78:712-7. [PMID: 21177138 DOI: 10.1016/j.saa.2010.11.054]

[26] Alabresm A, Chandler SL, Benicewicz BC, Decho AW. Nanotargeting of resistant infections with a special emphasis on the biofilm landscape. Bioconjug Chem 2021;32:1411-30. [PMID: 34319073 DOI: 10.1021/acs.bioconjchem.1c00116]

[27] Rana R, Awasthi R, Sharma B, Kulkarni GT. Nanoantibiotic formulations to combat antibiotic resistance - old wine in a new bottle. Recent Pat Drug Deliv Formul 2019;13:174. [PMID: 31544718 DOI: 10.2174/1872211313666190911124626]

[28] Phillips LC, Puett C, Sheeran PS, Wilson Miller G, Matsunaga TO, et al. Phase-shift perfluorocarbon agents enhance high intensity focused ultrasound thermal delivery with reduced near-field heating. J Acoust Soc Am 2013;134:1473. [PMID: 23927187 DOI: 10.1121/1.4812866]

[29] Kripfgans OD, Fowlkes JB, Miller DL, Eldevik OP, Carson PL. Acoustic droplet vaporization for therapeutic and diagnostic applications. Ultrasound Med Biol 2000;26:1177-89. [PMID: 11053753 DOI: 10.1016/s0301-5629(00)00262-3]

[30] Ho YJ, Huang CC, Fan CH, Liu HL, Yeh CK. Ultrasonic technologies in imaging and drug delivery. Cell Mol Life Sci 2021;78:6119-41. [PMID: 34297166 DOI: 10.1007/s00018-021-03904-9]